

Maximilian Passmann

Department of Mechanical Engineering,
University of Applied Sciences Muenster,
Steinfurt 48565, Germany
e-mail: max.passmann@fh-muenster.de

Stefan aus der Wiesche

Department of Mechanical Engineering,
University of Applied Sciences Muenster,
Steinfurt 48565, Germany
e-mail: wiesche@fh-muenster.de

Thomas Povey

Department of Engineering Science,
University of Oxford,
Oxford, OX1 3PJ, UK
e-mail: thomas.povey@eng.ox.ac.uk

Detlef Bergmann

SVMtec GmbH,
Stuttgart 70563, Germany
e-mail: bergmann@svm-tec.de

Effect of Reynolds Number on Five-Hole Probe Performance: Experimental Study of the Open-Access Oxford Probe

There is relatively little literature concerning the effect of Reynolds number on multi-hole aerodynamic probe performance. In particular, there is almost no discussion in the literature regarding the underlying mechanisms of Reynolds number (Re) sensitivity for such probes. In order to close this gap, detailed investigations of the effect of Re on a five-hole probe have been performed using both particle image velocimetry (PIV) techniques and oil flow visualizations. Wind- and water-tunnels were used to cover a wide range of Re . The open-access Oxford Probe was used for these studies because of the readily available data-sets and processing routines and to allow future comparisons by other authors. Complex flow dynamics including flow separation and re-attachment were identified, which cause Re -sensitivity of the calibration map at low Re even for low yaw or pitch angles. By comparing calibration maps across a wide range of Re , we demonstrate that the Oxford Probe can be employed without much loss of accuracy at lower Re levels than initially (conservatively) suggested, and quantify the errors in the extreme low- Re regime. Overall, we demonstrate the robustness of the Oxford Probe concept across a wide range of Re conditions, we more clearly defined the low- Re limit for the probe design and quantify errors below this limit, and we illustrate the fundamental mechanisms for Re -sensitivity of multi-hole probes. [DOI: 10.1115/1.4050597]

Keywords: measurement techniques, turbine blade and measurement advancements

Introduction

Multi-hole (pressure) probes can be used to measure flow angle, total and static pressure, dynamic pressure, and velocity (or Mach number) [1]. There are numerous multi-hole probe designs optimized for different applications. Perhaps the most common type, in applications where the entire flow structure is to be assessed, is the five-hole probe, which is widely used in turbomachinery surveying applications. Turbomachinery flows are generally characterized by Reynolds numbers in the range $10^5 < Re_L < 10^7$, where we set L to an arbitrary value of order 50 mm, which is of the order of the chord length of a nozzle guide vane or rotor blade [2,3]. This represents a Mach number range of $0.3 < M < 1.3$. In order to resolve details of such flows, probes of small physical size are desired. Probe tips of diameter $D = 3$ mm or smaller are not uncommon. The equivalent probe Reynolds number range based on tip diameter (for a 3 mm tip) is $6 \times 10^3 < Re_D < 6 \times 10^5$. In certain cases (e.g., tip-leakage flow investigations, or detailed wake traverses), even smaller probes have been used, with tip sizes as small as 0.6 mm [4], implying a Reynolds number as low as $Re_D = 1600$. In general, the desired probe tip size is determined by the smallest flow features to be resolved, but the practical probe tip size is limited by the mechanical requirements of the probe, as well as the required frequency response. The mechanical requirements are easily determined on a case-by-case basis. The requirements for frequency response have been well covered (e.g., [5,6]). There are known to be Reynolds number sensitivities at low Reynolds numbers (e.g., [3]), but this effect is poorly covered in the literature. A direct solution where low- Re operation is required is to calibrate

at several Re and employ a Re -sensitive calibration map during data processing. This significantly increases the complexity and cost. In many cases, the required effort and complexity would prohibit the use of a multi-hole probe.

The concept of using both additive manufacturing and a common calibration map (pre-determined based on calibrations for identical geometries) to dramatically lower the complexity and cost of multi-hole probes was explored by Hall and Povey [7] who proposed and developed an open-access five-hole probe. This was called the Oxford Probe, for which the design, manufacture files, calibration, and processing routines are available under a creative commons license (free for non-commercial use). The authors demonstrated that in many incompressible applications, the additive manufacturing process with a common calibration map delivers results of comparable accuracy to well-calibrated conventional probes. This allows for significant savings in cost and time, avoiding the need for conventional machining and individual calibration.

During the development of the Oxford Probe, it was observed that the Reynolds number sensitivity of the calibration map was small for $Re_D > Re_{D,crit} = 1.5 \times 10^4$ [7]. This Reynolds sensitivity threshold is in accordance with previous research (e.g. [3]). In practice, this might limit application of the probe in some low-speed environments. Two distinct Reynolds numbers effects are reported in literature: (i) flow separation around the probe head affects the performance at relatively low Reynolds numbers [3,8–11] and (ii) at low Reynolds numbers there is still a sensitivity indicated by static pressure variations even for the nulled cone-type probe [3,12]. Although these effects are known, there is little literature in which they are systematically studied and characterized (as function of Re). In this paper, we study in detail the flow structure changes that occur with Re and characterize the changes in the calibration map for relatively low- Re flows.

This paper is organized as follows: the Oxford Probe concept, design, and calibration maps are introduced; the wind

Contributed by the International Gas Turbine Institute (IGTI) of ASME for publication in the JOURNAL OF TURBOMACHINERY. Manuscript received November 16, 2020; final manuscript received February 18, 2021; published online May 3, 2021. Tech. Editor: David G. Bogard.

tunnel and water tunnels used in this study are described; a manufacture-through-to-calibration check of the Oxford Probe is performed as an independent assessment of the quoted errors; a systematic study of the change in the calibration map with Re is performed and the error maps discussed in detail; a detailed unsteady flow field analysis is performed to improve understanding of the underlying aerodynamic mechanisms.

Probe and Experimental Setups

Oxford Probe Design. The Oxford Probe is a five-hole pyramid probe of the design shown in Fig. 1. The pyramidal tip has an included angle of $\psi = 90$ deg, with sharp edge facets to minimize sensitivity to Reynolds number. The pyramid tip intersects a shallow cone with an included angle of $\phi = 14.2$ deg. A comprehensive description of the design and links to the resources associated with the probe, has been given by Hall and Povey [7].

For the present study, a probe with a tip diameter of $D = 4$ mm was used, which represents the lower limit recommended by Hall and Povey [7]. For lower tip diameters, the surface roughness and tolerances of the additive manufacturing process result in high errors when using the supplied common calibration map. The probe tip was manufactured in stainless steel (EOS StainlessSteel 316L, 18Cr-14Ni-2.5Mo) by means of Direct Metal Laser Sintering (DMLS). According to information provided by the supplier, a minimum wall thickness of 0.5 mm with a minimum feature size of 0.05 mm and a tolerance of 0.05 mm could be achieved. Figure 2 shows a photograph of the manufactured probe tip (before assembly onto an extension arm) and the corresponding three-dimensional scan. The scan (by means of a GOM ATOS Core optical 3D scanner) demonstrated that the probe tip was very close to the nominal geometry. The average deviations were found to be around ± 0.01 mm. In order to check the reproducibility

of the process, four additional probes were manufactured. Results were very similar to those of Fig. 2.

Calibration Fundamentals. Calibration methods for five-hole probes are well covered in the literature (e.g., [7]), but we briefly recite some fundamentals so the reader is familiar with the nomenclature used later in this paper.

The probe calibration procedure is that for each combination of pitch angle α and yaw angle β , the five probe hole pressures (p_1 to p_5 , see Fig. 1), as well as the wind tunnel jet total and static pressure (p_0 and p) are measured. The following calibration coefficients are then defined

$$\begin{aligned} C_\alpha &= \frac{p_1 - p_3}{p_5 - p_{avg}}, & C_\beta &= \frac{p_2 - p_4}{p_5 - p_{avg}}, \\ C_{p_s} &= \frac{p_{avg} - p}{p_5 - p_{avg}}, & C_{p_0} &= \frac{p_5 - p_0}{p_5 - p_{avg}} \end{aligned} \quad (1)$$

where p_{avg} is probe-frame proxy for static pressure, defined by

$$p_{avg} = \frac{1}{2} [\min(p_1, p_3) + \min(p_2, p_4)] \quad (2)$$

In the calibration environment, α , β , p , p_0 , and p_1 to p_5 (and hence p_{avg}) are all known, allowing the coefficients of Eq. (1) to be determined. Thus, calibration maps of the functional form $\alpha = \alpha(C_\alpha, C_\beta)$, $\beta = \beta(C_\alpha, C_\beta)$, $C_{p_s} = C_{p_s}(C_\alpha, C_\beta)$, and $C_{p_0} = C_{p_0}(C_\alpha, C_\beta)$ can be produced.

It should be noted for completeness that alternative definitions of p_{avg} are in use. For instance, Treaster and Yocum [13] prefer the average value $p_{avg} = (p_1 + p_2 + p_3 + p_4)/4$ instead of Eq. (2). In our study, following Hall and Povey [7], we use Eq. (2), because the well-known zero-denominator problem in Eq. (1) is pushed toward higher angles of attack, giving a larger usable angular range for the probe.

When the probe is used for measurements in an unknown flow, only pressure data p_1 to p_5 are available. Obtaining p_{avg} by means of Eq. (2), the coefficients C_α and C_β can be determined, allowing for a lookup of the flow angles α and β , as well as the coefficients C_{p_s} and C_{p_0} . Static and total pressures can then be determined from Eq. (1). The process is described in detail in Ref. [7].

Overview of Probe Calibration Facilities. We compare results gathered in two different calibration facilities: the Oxford Probe Calibration Facility (OPCF) (for details, see [7]); and the wind tunnel calibration facility at Muenster University of Applied Sciences (MUAS). The reference calibration map was obtained in the OPCF at a nominal Reynolds number of $Re_D = 8.0 \times 10^4$ and a Mach number of 0.3 [7]. An independent calibration at similar conditions was performed at MUAS, as well as calibrations over an extended range of Re (at the low-Re end of the range). The MUAS facility is now described.

The MUAS calibration facility is an open circuit, atmospheric wind tunnel. The jet flow uniformity and turbulence intensity were determined by means of hot-wire probe traverses. The values were found to be of order 0.1% up to 0.3%. A schematic of the wind tunnel with its traverse system are shown in Fig. 3. The jet has a rectangular cross section (450 mm \times 150 mm); hence, the blockage effect due to the probe was negligible. The traverse system consists of two rotational axes, each driven by stepper motors and high-ratio synchronous belt drives with a positioning accuracy of 0.2 deg. The calibration range was ± 40 deg in steps of $\Delta\alpha = \Delta\beta = 4$ deg. A summary of the experimental uncertainty level of the sensors is given in Table 1. The jet velocity V_∞ and therefore Reynolds number Re_D were controlled by the running speed of a centrifugal blower. All experiments were conducted in the incompressible range of Mach number ($0 < M \leq 0.2$). Oil flow visualizations were conducted using a large-scale model of the probe ($D = 20$ mm), as we discuss later.

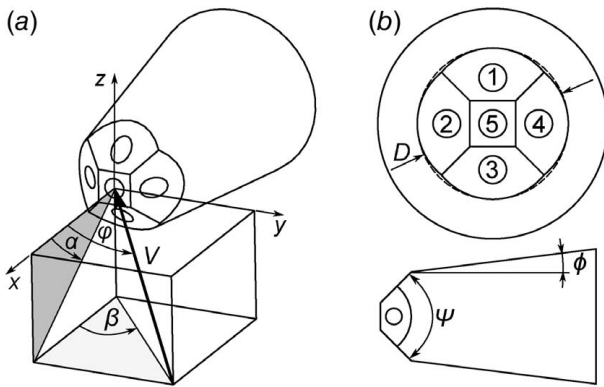


Fig. 1 (a) Schematic of the probe tip showing flow angle convention and (b) design of Oxford Probe with hole numbering

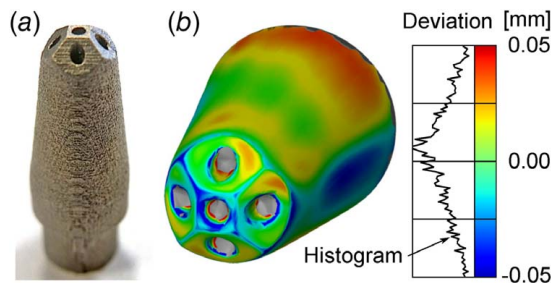


Fig. 2 (a) Photograph of DMLS probe tip and (b) deviation analysis of the 3D scanned probe tip including histogram

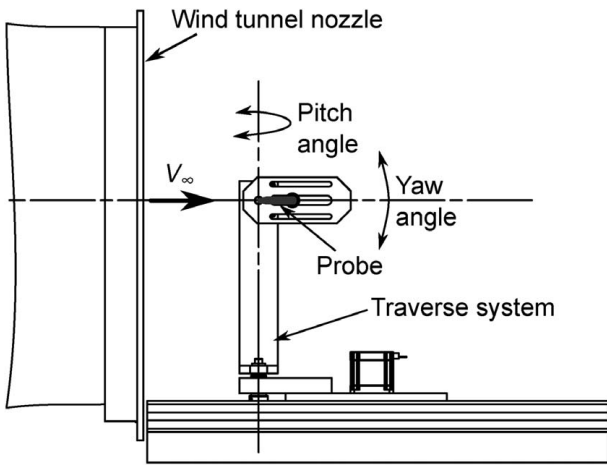


Fig. 3 Schematic of the MUAS calibration facility showing the two (rotational) axis traverse system

Table 1 Uncertainty summary for the MUAS calibration facility instrumentation

	Sensor model	Total range (Pa)	Relative uncertainty (%)
p_1, \dots, p_5	SVMtec	± 2500	0.25
	PSC5-OX		
p_0	H&W P26	± 2500	0.2
p	H&W P26	± 50	0.2
p_∞	Wika P-30	$0.8 - 1.2 \times 10^5$	0.1

Water Tunnel and Particle Image Velocimetry Measurement System. Particle image velocimetry (PIV) studies of flow around the probe tip were conducted in a closed-circuit water tunnel facility at Muenster University of Applied Sciences. A schematic of the test section is shown in Fig. 4. Flow speed was controlled by means of an adjustable valve and could be varied up to 0.8 m/s (demineralized water at room temperature). The test section cross section was 160 mm \times 160 mm, and the probe diameter $D = 20$ mm. The blockage factor was between 3% and 10%, depending on the probe orientation within the test section. PIV illumination was carried out with a continuous solid state line laser with a wavelength of $\lambda = 532$ nm. Image capture was with a CMOS high-speed camera (frame rate up to 4000 frames/s) in multi-frame/single-exposure mode [14]. For post-processing PIVlab (version 2.20) for MATLAB was employed [15]. Hollow glass spheres recommended for water tunnel applications due to their low velocity lag [14] with a mean diameter of 10 μ m were used as tracer particles.

Calibration Maps and Errors

We now compare the reference (OPCF) and independent (MUAS) calibration maps and discuss the impact of Reynolds number on the calibration. A detailed flow analysis using PIV and oil-flow visualizations is presented thereafter.

Independent Check of the Oxford Probe Calibration. In this section, we report an independent check of the Oxford Probe calibration map, using data from the MUAS calibration facility. This repeats work performed by Hall and Povey [7], to provide independent validation of the Oxford Probe method.

This is relevant because the Oxford Probe concept is based on the idea that probes can be manufactured using any high quality DMLS process and used with a common calibration map, i.e., without individual calibration. This independent check was performed (see [16]) prior to any collaboration with the original team and thus represents

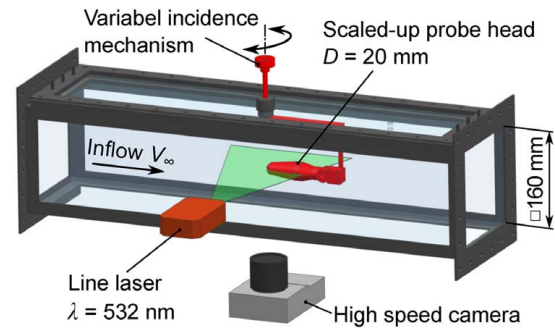


Fig. 4 Schematic of the water tunnel test setup for the PIV investigation

a complete process-check of the Oxford Probe. The independent calibration was performed at $Re_D = 1.5 \times 10^4$, which was exactly at the lower limit of the range suggested for use of the probe ($Re_{D,crit} = 1.5 \times 10^4$, see [7]).

The independent calibration was in very good agreement with the calibration files provided for the Oxford Probe [7]. We define errors as the difference between angles, total pressures, and dynamic head values returned by the reference and independent calibration maps as follows:

$$\begin{aligned} \epsilon_\alpha &= \alpha_{ref} - \alpha, & \epsilon_\beta &= \beta_{ref} - \beta, \\ \epsilon_{p_0} &= \frac{|p_{0,ref} - p_0|}{p_0}, & \epsilon_q &= \frac{|q_{ref} - q|}{q} \end{aligned} \quad (3)$$

RMS values for these quantities were evaluated across the entire map (± 40 deg in both axes) along lines of data for constant compound angle φ . The definition of the compound angle φ is illustrated in Fig. 1. For calculating the RMS values, the resolution of the compound angle lines was 1 deg.

With the exception of the dynamic pressure error, the resulting RMS values are within the ranges quoted in Ref. [7], validating the entire process of Oxford Probe use by an independent team. The larger-than-expected error for dynamic pressure is explained by high uncertainty in the static pressure measurements used in the MUAS tunnel. It is believed that better instrumentation would improve this result.

For completeness, we note that precise roll-alignment for probes of small diameter can be very difficult to achieve in practice (for discussion, see [7]). It was found (see [16]) that errors could be reduced further with a roll corrections of 2.5 deg, within the accuracy of the probe set-up. Likewise, systematic misalignment of order 1 deg (in pitch or yaw) is realistic in most applications and should be considered.

Comparison of Calibration Maps at Several Re_D . Calibration maps in the range $2 \times 10^3 \leq Re_D \leq 1.5 \times 10^4$ where produced at MUAS and compared with the reference Oxford Probe calibration map ($Re_D = 8.0 \times 10^4$). The purpose was to quantify deviations from the reference calibration map for $Re_D < Re_{D,crit} = 1.5 \times 10^4$. Results are plotted in Fig. 5.

As reported in the previous section, deviations between the measured calibration map at the highest Re (MUAS $Re_D = 1.5 \times 10^4$) and the reference calibration map (Oxford University (OX) $Re_D = 8 \times 10^4$) were found to be small, and generally (one exception discussed above) within the quoted errors in the Oxford Probe paper [7]. Examining the calibration maps, we see excellent agreement between measurement and reference for both pitch and yaw angle maps and very good agreement for total and static pressure calibration maps.

We take this result as an independent validation of the claimed accuracy of the overall technique reported in Ref. [7], including the fact that it is realistic to build probes to within the required tolerances using typical high-accuracy DMLS techniques. To examine

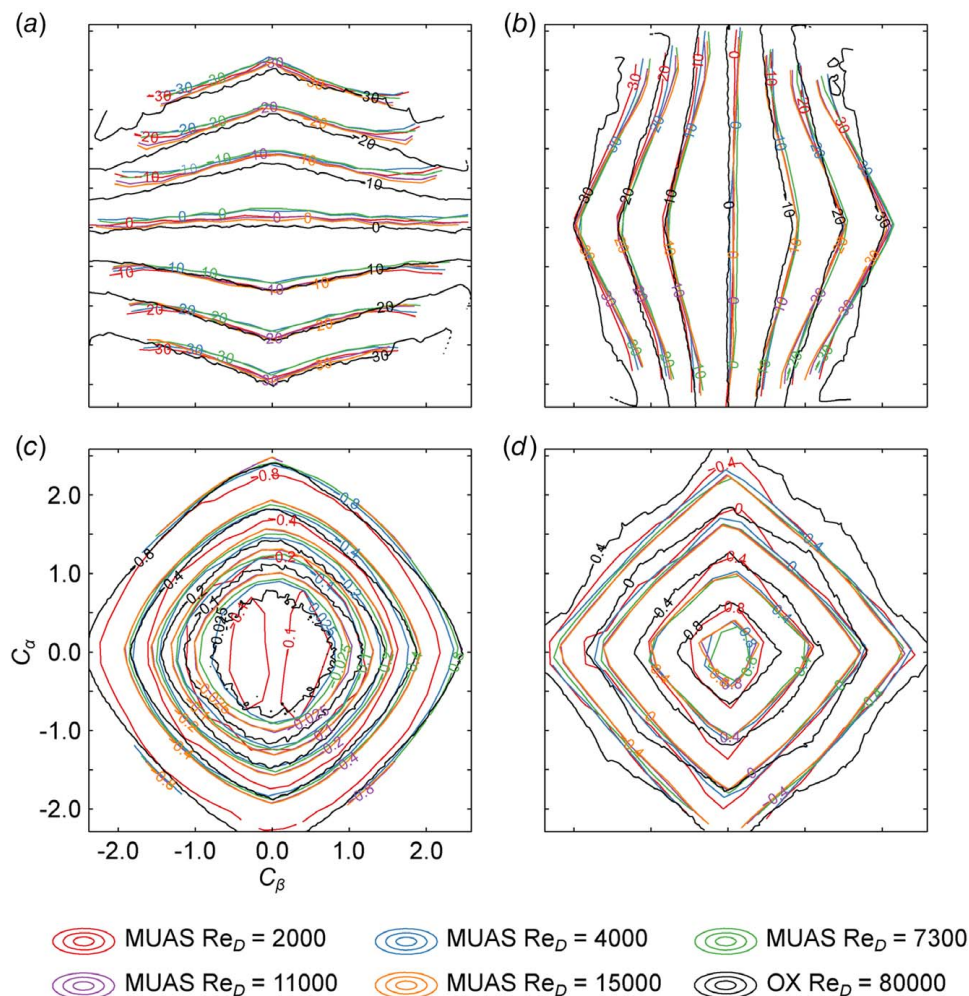


Fig. 5 Calibration maps at six different Reynolds numbers for a 4 mm DMLS Oxford Probe: (a) pitch angle α , (b) yaw angle β , (c) total pressure coefficient C_{p0} , and (d) static pressure coefficient C_{ps}

the variation with Re in isolation, we now take the map from the MUAS calibration facility at the highest Re ($MUAS\ Re_D = 1.5 \times 10^4$) as the reference for examining the sensitivity to Re .

Figure 6 shows Re sensitivity of the Oxford Probe in terms of coefficients C_α , C_β , C_{p0} , and C_{ps} as a function of both pitch angle (for two fixed yaw angles of 0 deg and 35 deg) and yaw angle (for two fixed pitch angles of 0 deg and 35 deg). Results are shown for four values of Re_D . These particular intersections of the calibration maps are used to visualize the deviations in the maps, but we later present RMS values as a holistic measure of the deviation. The red band in Fig. 6 denotes the experimental uncertainty level for the lowest Reynolds number (for higher Reynolds numbers, the uncertainty level was much smaller and remained essentially within the plotted lines).

Reynolds number sensitivity of C_α and C_β is small, and lines for all Re_D conditions essentially collapse to a single characteristic (top row in Fig. 6). Reynolds number sensitivity of C_{p0} (middle row in Fig. 6) is moderate, and for $Re_D = 2000$ in particular there is a significant deviation (up to $\Delta C_{p0} \approx 0.3$) from the reference map for this study. The Re sensitivity of C_{ps} (bottom row of Fig. 6) is much weaker. These results are in qualitative agreement with Dominy and Hodson [3].

We now quantify the deviations between the maps by providing RMS deviation between each particular map and the reference map ($MUAS\ Re_D = 1.5 \times 10^4$) as a function of compound angle φ . These data are shown in Fig. 7. The RMS deviations for $Re_D = 1.5 \times 10^4$ are identical to zero by definition. For $Re_D = 1.1 \times 10^4$, the RMS

deviation between maps is very small, remaining below 1 deg for both α and β , and below 1% for p_0 and 2% for q over a compound angle range of 0 deg $< \varphi < 35$ deg. These errors are small and well within the typical error range of a well-calibrated probe. For $Re_D = 7.3 \times 10^3$, the RMS deviation between maps is moderate, remaining below 3 deg for both α and β , and below 5% for p_0 and 10% for q over a compound angle range of 0 deg $< \varphi < 35$ deg. For angle determination, this may be acceptable in some applications, but is unlikely to be adequate in terms of accuracy of p_0 and q without individual calibration.

For $Re_D = 4.0 \times 10^3$ and $Re_D = 2.0 \times 10^3$, the errors in angle determination remain similar (within 5 deg for both α and β), but the errors in p_0 and q rise rapidly with decreasing Re_D , becoming especially pronounced at high compound angles. For $Re_D = 2.0 \times 10^3$ and $\varphi = 35$ deg errors in p_0 and q are approximately 20% and 45%, respectively. It is clear that there would be very few applications in which such errors could be regarded as acceptable.

To visualize the Reynolds number sensitivity of the Oxford Probe, error surfaces were computed and are shown as contour plots in Fig. 8. In line with the discussion around Fig. 7, we see that errors are negligible for all quantities at $Re_D = 1.1 \times 10^4$. For $Re_D = 7.3 \times 10^3$, some Reynolds number effects become visible, but their levels remain within the usual range of experimental uncertainty. For $Re_D = 4 \times 10^3$ and $Re_D = 2 \times 10^3$, the errors in total pressure and dynamic head are significant, demanding an individual calibration in the Re_D range. Interestingly enough, the errors in pitch and yaw angles were still relatively small down to

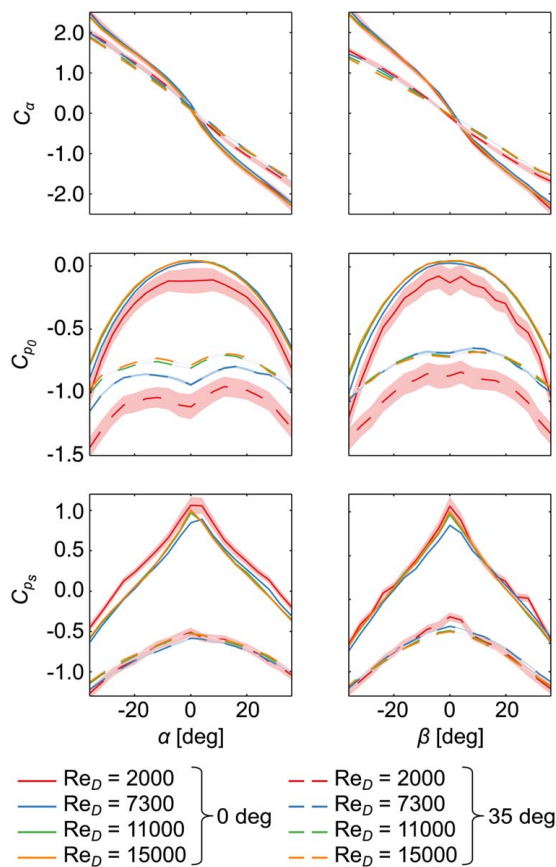


Fig. 6 Effect of Reynolds number on calibration coefficients. Colored bands denote experimental uncertainty.

$Re_D = 2 \times 10^3$, and perhaps usable where only indicative measurements are required, particularly at low compound angle.

Results of the Flow Field Analysis

Detailed flow field investigations were performed to better understand the physical mechanisms for the changes in calibration map at

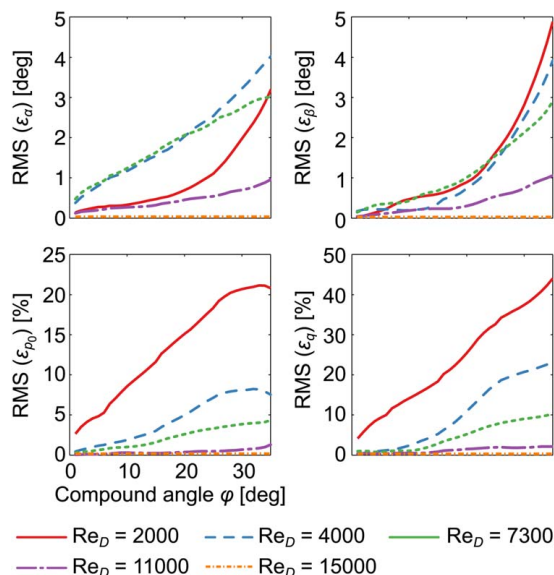


Fig. 7 Root-mean-squared errors due to Reynolds number effect as a function of the compound angle ϕ

low Re_D . As typical examples of flow in the high-Re regime (calibration map insensitive to Re) and the low-Re regime (calibration map significantly altered by low-Re effects), we present and compare data for $Re_D = 1.1 \times 10^4$ and $Re_D = 2.2 \times 10^3$. We first consider unsteady PIV measurements showing flow structure, then oil flow visualizations showing surface streamline pattern, and finally the unsteady pressure distribution.

Unsteady Flow Visualization Using Particle Image Velocimetry. Streamlines were obtained in the water tunnel by long-time exposure of a large-scale ($D = 20$ mm) model of the probe. Some representative results for $Re_D = 1.1 \times 10^4$ and $Re_D = 2.2 \times 10^3$ are shown in Fig. 9, for three angles of attack. The general picture is that flow is stagnated on the leading flat of the probe, attached on the 45 deg facets (up to an angle of attack of 30 deg), and separated (note separation bubble and flow reattachment) from the intersection with the conical body. Importantly, both the position of the dividing streamline and the size of the separation bubble depend on both incidence angle and Reynolds number. That is, the flow structure is significantly altered between $Re_D = 1.1 \times 10^4$ and $Re_D = 2.2 \times 10^3$. Changes in the calibrations maps are therefore to be expected.

The nature of the flow separation was further investigated by PIV measurements with high temporal resolution. Based on the velocity fields obtained by PIV, the vorticity

$$\omega = \nabla \times \mathbf{V} \quad (4)$$

was computed and used for calculating the dimensionless vorticity

$$\omega^* = \frac{\omega D}{V_\infty} \quad (5)$$

A time-sequence of eight consecutive images is presented in Fig. 10, showing vortex shedding from the intersection with the conical main body. To enable vortex tracking, the vortices are numbered in the figure. We will see in a later section that the characteristic shedding frequency changes with Re_D and affects both the steady and unsteady pressure coefficient distribution around the probe tip.

Surface Streamline Pattern Using Oil Flow Technique. To provide insight into the surface flow behavior on the probe tip, surface oil flow visualizations were performed with the large-scale ($D = 20$ mm) model in the wind tunnel facility. Results of this visualization study are shown in Fig. 11.

Repeatable measurements were achieved for $Re_D \geq 7 \times 10^3$ (oil viscosity to shear ratio), and therefore, results are restricted to this range. Possibly the two most striking features of the flow visualization are the significant amounts of oil accumulation in re-circulation bubbles at high angles of incidence, and the wakes that form around individual holes. The latter is particularly interesting because there is no net inflow/outflow from the holes. It is speculated that the wakes form in a similar manner to the so-called synthetic jet effect, in which the pulsation causes an effective separation bubble. These features are Re-dependent as indicated by the different oil patterns for a given probe orientation. Although the main qualitative behavior of the oil pattern is similar for all Reynolds numbers considered in Fig. 11, the size of the oil accumulation zone depends on the actual Reynolds number.

Time-Average Pressure Coefficient Distributions. We define a pressure coefficient

$$C_p = 1 - \left(\frac{V}{V_\infty} \right)^2 \quad (6)$$

where V is the velocity magnitude and V_∞ is the (approximately steady) free-stream velocity magnitude. A time-average pressure

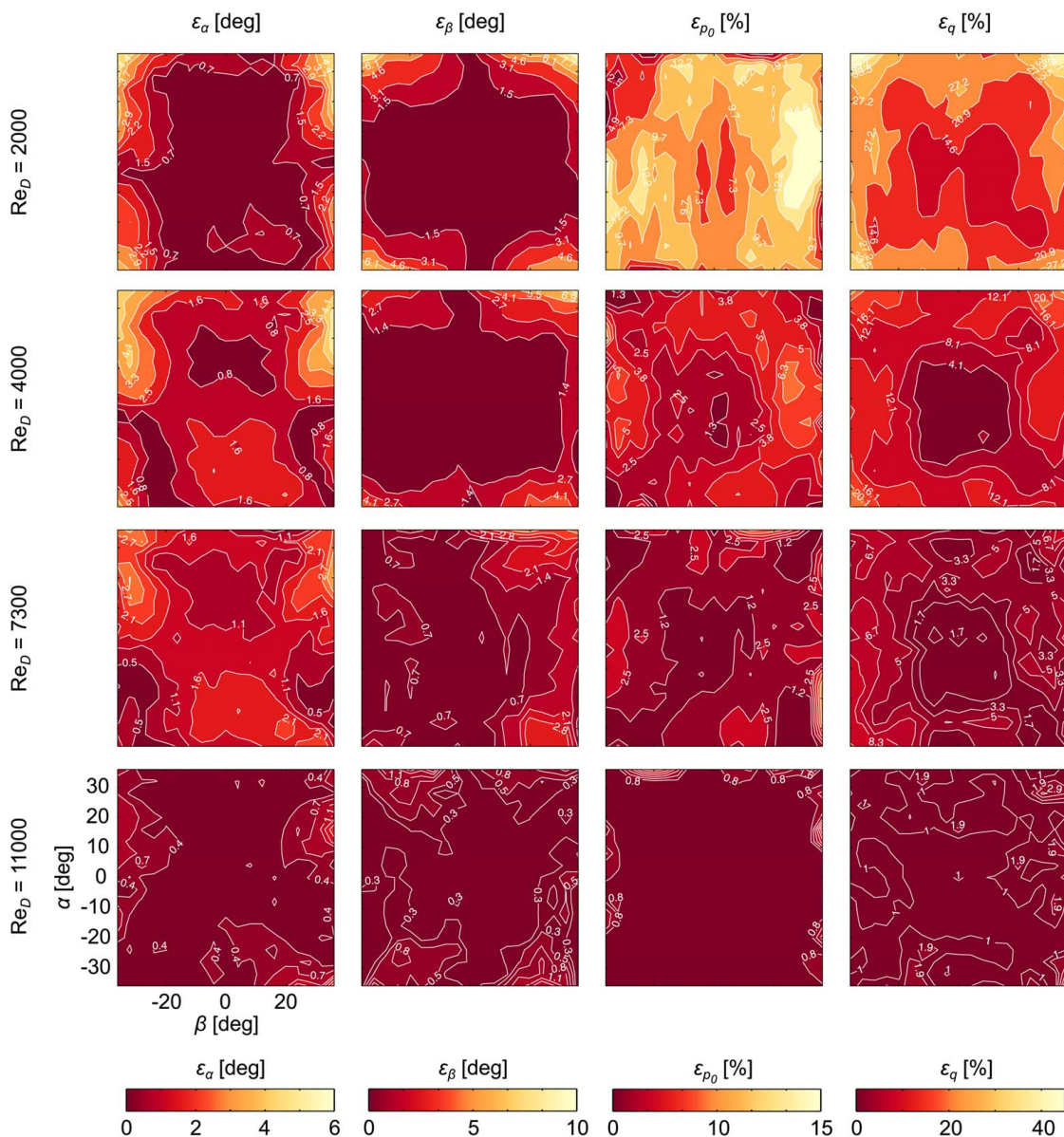


Fig. 8 Error surfaces (difference to reference calibration map at $Re_D = 15,000$) for pitch and yaw angles, total pressure, and dynamic pressure at four different Reynolds numbers

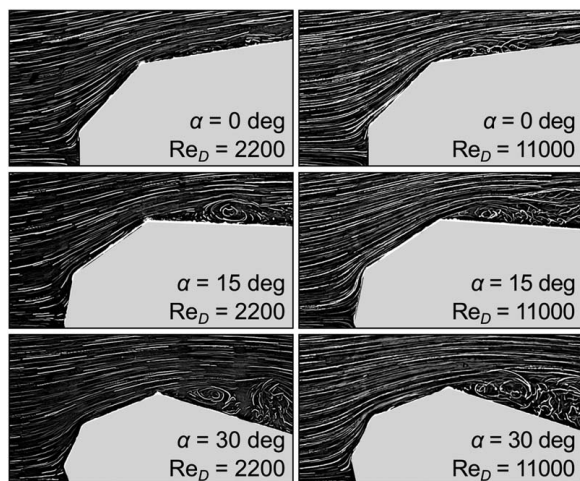


Fig. 9 Streamlines for two Reynolds numbers and different angles of attack

coefficient \bar{C}_p can be obtained by inserting the time-average velocity magnitude field \bar{V} into Eq. (6). In addition, an unsteady (instantaneous) pressure coefficient C_p is obtained in the following using the local time-instantaneous values for the velocity magnitude V . The difference between this time-average pressure coefficient and a quantity based on averaging the sample of instantaneous pressure coefficient distributions is negligible in order to illustrate the resulting flow field as done in Fig. 12.

Contours of the time-average pressure coefficient obtained for $Re_D = 2.2 \times 10^3$, 4.3×10^3 , 7.0×10^3 , and 1.1×10^4 are shown in Fig. 12. The dominant features are the stagnation flow on the leading flat, a region of flow acceleration around the probe tip, and a separation (with associated constant static pressure region) from the conical main body of the probe. The wake caused by separation gives a first-order change in the velocity field, even at the stagnation point, an effect well-studied in the case of flow past cylinders and spheres [17], but common for all blunt bodies. The primary change in flow structure with angle is the movement of the stagnation point and an increase in the shape of the main separation bubble. For the two highest values of $Re_D = 7.0 \times 10^3$ and 1.1×10^4 , the pressure coefficient distributions

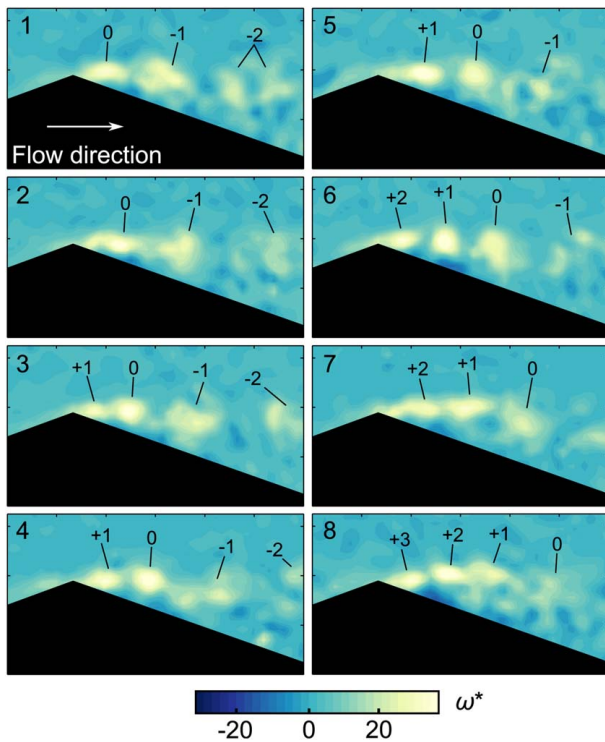


Fig. 10 Ordered sequence of dimensionless vorticity contours at equal time intervals ($Re_D = 4300$, $\alpha = 30$ deg)

are similar, but there are noticeable changes, in particular in the shape and magnitude of the low-pressure bubble ($\bar{C}_p < -0.5$) at lower Re_D , with pronounced changes for $Re_D = 2.2 \times 10^3$. This is in accordance with the results of Figs. 8 and 9, which show changes in the calibration maps and in the shape of the separation bubble, respectively.

The change in separation with Re is analyzed in Fig. 13, in which time average pressure coefficient distributions on the probe surface are plotted for $Re_D = 2.2 \times 10^3$ and $Re_D = 1.1 \times 10^4$, each for two angles of attack ($\alpha = 0$ deg and 30 deg). On the leading flat ($s < L_1$), there is little change with changing Re_D . Beyond the first and second facets however ($s > L_1$, and $s < L_1 + L_2$, respectively), there is a significant change in the pressure coefficient with Re_D , both in terms of the location and peak magnitudes. This is also shown in Fig. 12.

Unsteady Pressure Coefficients. Using the unsteady PIV data, the pressure coefficient signals were evaluated in more detail in the vicinity of hole 5 and hole 1 (see Figs. 1 and 13). Time resolved data are presented in Fig. 14 for two different Reynolds numbers and angles of attack. The grey line corresponds to hole 5, and the black line to hole 1. In line with the time-average data of Figs. 12 and 13, there is a small but measurable difference in the mean pressure coefficient value when moving from low to high Re_D . There is significantly greater unsteadiness in the pressure coefficient at hole 1 (black lines) than at hole 5 (grey lines). This is in accordance with the results of Fig. 10, which shows that the unsteady potential field impact of the vortex shedding is greater at the side hole (hole 1) than in the tip region. Furthermore, Fig. 14 demonstrates that the amplitude of the unsteadiness is greater for $Re_D = 1.1 \times 10^4$ than for $Re_D = 2.2 \times 10^3$.

Power spectral densities (PSDs) of the unsteady pressure coefficients were obtained by means of Fast-Fourier-transforms (FFT). Results are shown in Fig. 15. The dominant trend in all plots is a decrease in PSD with increasing frequency. For the low- Re flow, $Re_D = 2.2 \times 10^3$, this was reasonably well-correlated by a power law with an exponent of $-1/2$ (indicated by a dotted line $f^{-1/2}$ in Fig. 15). For the higher Reynolds number flow, $Re_D = 1.1 \times 10^4$, the trend was in agreement with the well-known $1/f$ spectrum for the so-called pink noise. In the case of transient measurements at higher frequencies, this subtle effect of Reynolds number on the transfer function of a probe might be of some interests.

For low- Re flow at high angle of attack ($\alpha = 30$ deg), a local peak at about $f = 30$ Hz was identified (the same was observed

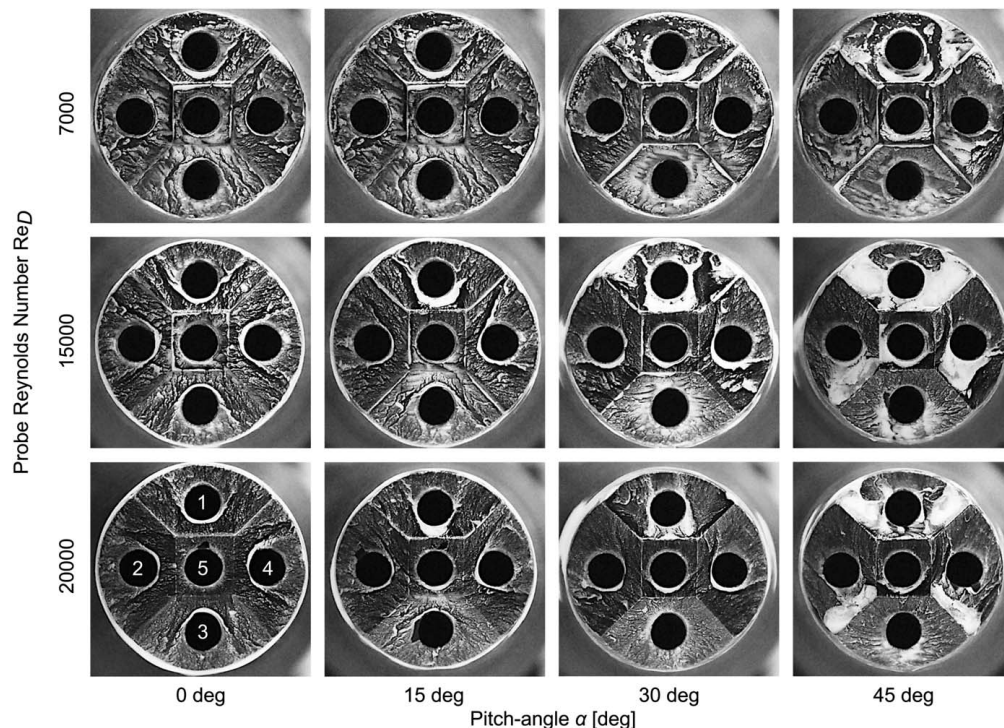


Fig. 11 Surface oil flow visualizations for different probe Reynolds numbers and pitch angles

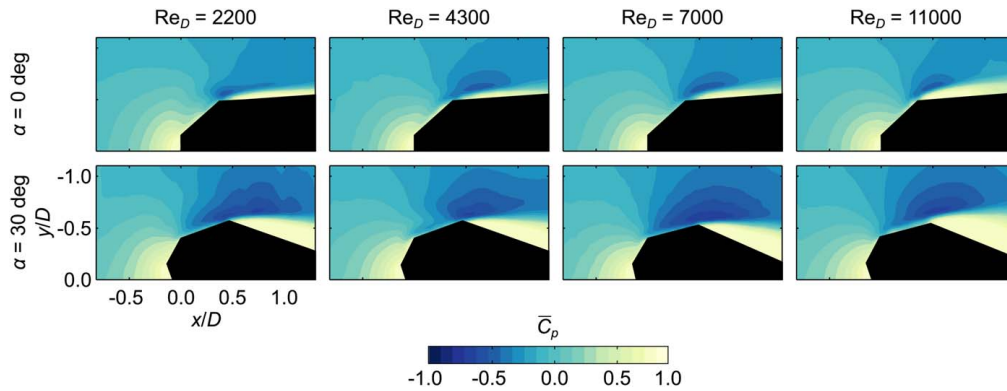


Fig. 12 Time average pressure coefficient \bar{C}_p for different Reynolds numbers and angles of attack

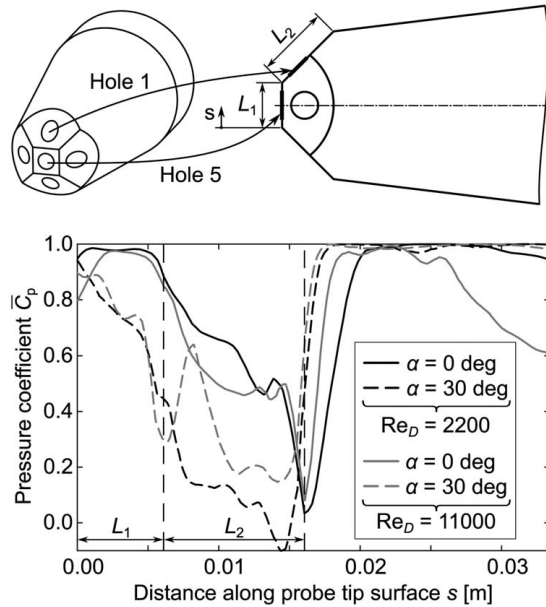


Fig. 13 Time average pressure coefficient on probe surface as function of Reynolds number (definition of distance s as shown in sketch above)

for $Re_D = 2.2 \times 10^3$, $\alpha = 15$ deg, but is not presented here), in accordance with the results of Fig. 10, which show vortex shedding. For the higher Reynolds number flow, $Re_D = 1.1 \times 10^4$, the regular vortex shedding seemed to be replaced by a more chaotic flow, and no dominant peak due to vortex shedding was observed.

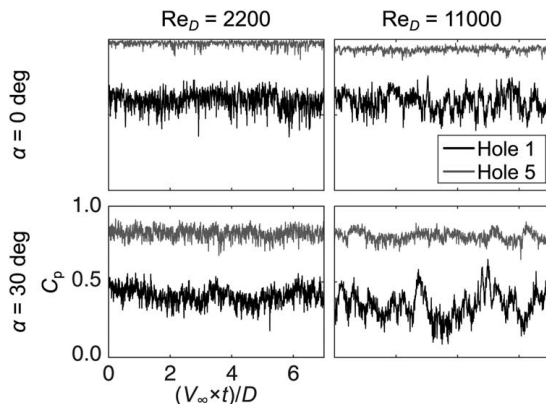


Fig. 14 Time resolved pressure coefficient in the vicinity of hole 5 (tip) and hole 1 (side)

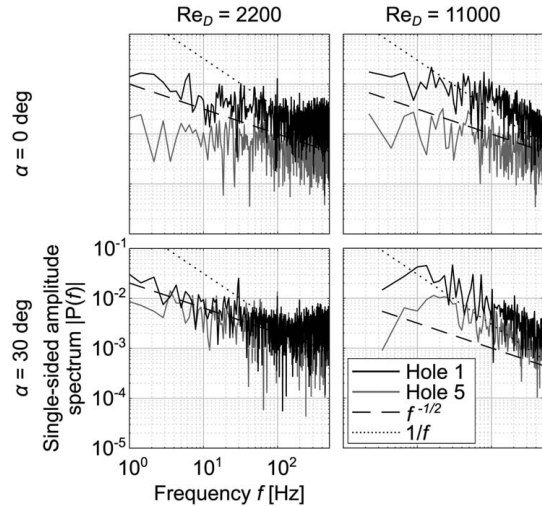


Fig. 15 Unsteady pressure coefficient power spectral density for hole 5 (tip) and hole 1 (side)

Conclusions

Five-hole aerodynamic probes have been used by engineers and researchers since the late 1950s. A number of different tip designs are in common use (hemispherical, conical, pyramidal, etc.), and although these exhibit similar behavior, it has been argued (with good physical basis, e.g. [3,10]) that faceted probes should exhibit less Re-sensitivity than their un-faceted counterparts (hemispherical, for example). There is, however, relatively little literature supporting this assertion or providing clear guidelines for the low-Re limits for various probe types.

In one of the most detailed studies of its type, we systematically characterize changes in calibration map below the typical low-Re limit as well as the changing structure of the flow field. For the latter, we carried out detailed analysis of the surface flow field (via oil-flow visualization, Fig. 11) and the time average (Figs. 12 and 13) and unsteady (Figs. 14 and 15) pressure coefficient distributions. We show that the nature of the flow separation is similar over a very wide range of Re (from $Re_D = 2.2 \times 10^3$ upwards), but that below a Re-limit of approximately $Re_D = 1.1 \times 10^4$, subtle changes in the flow structure, including the shape, size and characteristic frequency spectrum of the separation, cause changes in the calibration map.

As an independent verification study (different researchers, calibration facility, and manufacture method) of the open-access Oxford Probe [7] concept, we have shown that for $Re > Re_{D,crit} = 1.5 \times 10^4$ the probe may be manufactured and used within the quoted errors of the original paper, without the need for individual

calibration. This is a powerful concept, as it significantly reduces the complexity and cost of implementing multi-hole probe measurements in many environments.

By extensive calibrations at a range of Re_D , we have extended the Oxford Probe work to demonstrate that the probe can be used without significant loss of accuracy down to $Re_D = 1.1 \times 10^4$ (a little lower than previously thought), and where only moderate accuracy is required, to values as low as $Re_D = 7.0 \times 10^3$ (RMS deviation between maps remains below 3 deg for both α and β , and below 5% for p_0 and 10% for q over a compound angle range of $0 \text{ deg} < \varphi < 35 \text{ deg}$).

It is hoped that the work can now be extended to develop a user-friendly compact probe system, including an integrated signal processing unit, to allow reduction of flow variables for indicative purposes without the need for individual calibration or further data processing.

Acknowledgment

The support of the student Marius Leetz during calibration at MUAS and the contributions of the student David Zeemann during the PIV study are acknowledged.

The authors are grateful to Ms Lina Masour who started the PIV analysis of the probe during her academic exchange program funded by the program NRW-Israel-Palästina-Jordanien.

Conflict of Interest

There are no conflicts of interest.

Data Availability Statement

The authors attest that all data for this study are included in the paper. Data provided by a third party are listed in Acknowledgment.

Nomenclature

f	= frequency, Hz
q	= dynamic pressure, Pa
\mathbf{V}	= velocity vector, m/s
D	= probe body nominal diameter, m
L	= length, m
V	= velocity magnitude, m/s
p_0	= total pressure, Pa
$p_{1,\dots,5}$	= pressure as measured by probe holes 1–5, Pa
p_{avg}	= probe-based proxy for static pressure, Pa
C_p	= pressure coefficient
p, p_s	= static pressure, Pa
$C_\alpha, C_\beta, C_{p_0}, C_{p_s}$	= probe calibration coefficients
Re_D	= probe Reynolds number
$Re_{D,crit}$	= critical Reynolds number

Greek Symbols

α	= pitch angle, deg
β	= yaw angle, deg
ε	= probe error
ν	= kinematic viscosity, m^2s^{-1}
ϕ	= probe body included angle, deg
φ	= compound angle, deg
ψ	= probe tip included angle, deg
ω	= vorticity, s^{-1}
ω^*	= dimensionless vorticity

References

- [1] Bryer, D. W., and Pankhurst, R. C., 1971, *Pressure-Probe Methods for Determining Wind Speed and Flow Direction*, H.M.S.O, London, UK.
- [2] Dixon, S. L., and Hall, C. A., 2013, *Fluid Mechanics and Thermodynamics of Turbomachinery*, 6th ed., Butterworth-Heinemann, Oxford, UK.
- [3] Dominy, R. G., and Hodson, H. P., 1993, "An Investigation of Factors Influencing the Calibration of Five-Hole Probes for Three-Dimensional Flow Measurements," *ASME J. Turbomach.*, **115**(3), pp. 513–519.
- [4] Yamamoto, A., 1989, "Endwall Flow/Loss Mechanisms in a Linear Turbine Cascade With Blade Tip Clearance," *ASME J. Turbomach.*, **111**(3), pp. 264–275.
- [5] Hall, B. F., and Povey, T., 2018, "A Practical Model for Pressure Probe System Response Estimation (With Review of Existing Models)," *Meas. Sci. Technol.*, **29**(4), p. 045301.
- [6] Burdett, D., Lubbock, R., and Povey, T., 2018, "An Impulse Response Technique to Improve the Effective Frequency Response of Pressure Probes," Proceedings of the XXIV Biannual Symposium on Measuring Techniques in Turbomachinery Transonic and Supersonic Flow in Cascades and Turbomachines, MTT - Measuring Techniques in Turbomachinery, Prague, Czech Republic, pp. 1–12.
- [7] Hall, B. F., and Povey, T., 2017, "The Oxford Probe: An Open Access Five-Hole Probe for Aerodynamic Measurements," *Meas. Sci. Technol.*, **28**(3), p. 035004.
- [8] Krause, L., and Dudzinski, T., 1969, "Flow-Direction Measurement With Fixed Position Probes in Subsonic Flow Over a Range of Reynolds Numbers," Proceedings of the 15th International ISA Aerospace Instrumentation Symposium, ISA, Las Vegas, NV, pp. 217–223.
- [9] Smith, L. A., and Adcock, J. B., 1986, Effect of Reynolds Number and Mach Number on Flow Angularity Probe Sensitivity. Technical Report, NASA TM-87750.
- [10] Wallen, G., 1983, "Reynolds Number Effects on Cone and a Wedge Type Pressure Probe," Proceedings of the 7th Symposium on Measuring Techniques in Transonic and Supersonic Flows in Cascade and Turbomachines, Aachen Germany, MTT - Measuring Techniques in Turbomachinery.
- [11] Koschel, W., and Pretzsch, P., 1988, "Development and Investigation of Cone-Type Five-Hole Probes for Small Gas Turbines," Proceedings of the 9th Symposium on Measuring Techniques in Transonic and Supersonic Flows in Cascade and Turbomachines, Oxford UK, MTT - Measuring Techniques in Turbomachinery.
- [12] Wallen, G., 1983, "Investigation of the Reynolds Number Effect of Two Pressure Probes for Measurements in Turbomachines," Proceedings of the 7th Symposium on Measuring Techniques in Transonic and Supersonic Flows in Cascade and Turbomachines, Aachen, Germany, MTT - Measuring Techniques in Turbomachinery.
- [13] Treaster, A. L., and Yocum, A. M., 1978, The Calibration and Application of Five-Hole Probes. Technical Report, Pennsylvania State University, University Park Applied Research Lab.
- [14] Raffel, M., Willert, C. E., Kähler, F., and Scarano, C. J., Wereley, S. T., and Kompenhans, J., 2018, *Particle Image Velocimetry: A Practical Guide*, Springer, Cham, Switzerland.
- [15] Thielicke, W., and Stamhuis, E., 2014, "PIVlab—Towards User-Friendly, Affordable and Accurate Digital Particle Image Velocimetry in MATLAB," *J. Open Res. Software*, **2**(1), pp. 1–10.
- [16] Voßschulte, C. H., 2013, "Erprobung Einer Open-Source Fünflochsonde: Die Oxford-Probe," Thesis, Muenster University of Applied Sciences, Steinfurt, Germany.
- [17] White, F. M., 2006, *Viscous Fluid Flow*, 3rd ed., Vol. 3, McGraw-Hill, New York.